Evolution of *L*-shell photoabsorption of the molecular-ion series SiH_n^+ ($n = 1,2,3$): Experimental and theoretical studies

E. T. Kennedy,[1] J.-P. Mosnier,[1,*] P. van Kampen,[1] J.-M. Bizau,[2,3] D. Cubaynes,[2,3] S. Guilbaud,[2]
S. Carniato,[4] A. Puglisi,[4] and N. Sisourat[4]

[1]*School of Physical Sciences and NCPST, Dublin City University, Dublin 9, Ireland*
[2]*Institut des Sciences Moléculaires d'Orsay, CNRS, Université Paris–Sud, and Université Paris–Saclay, F-91405 Orsay, France*
[3]*Synchrotron SOLEIL, L'Orme des Merisiers, Saint-Aubin, Boîte Postale 48, F-91192 Gif-sur-Yvette Cedex, France*
[4]*Sorbonne Universités, UPMC Univ Paris 06, CNRS, UMR 7614, Laboratoire de Chimie Physique-Matière et Rayonnement,
F-75005 Paris, France*

We report on complementary laboratory and theoretical investigations of the $2p$ photoexcitation cross sections for the molecular-ion series SiH_n^+ ($n = 1,2,3$) near the *L*-shell threshold. The experiments used an electron cyclotron resonance (ECR) plasma molecular-ion source coupled with monochromatized synchrotron radiation in a merged-beam configuration. For all three molecular ions, the Si^{2+} decay channel appeared dominant, suggesting similar electronic and nuclear relaxation patterns involving resonant Auger and dissociation processes, respectively. The total yields of the Si^{2+} products were recorded and put on absolute cross-section scales by comparison with the spectrum of the Si^+ parent atomic ion. Interpretation of the experimental spectra ensued from a comparison with total photoabsorption cross-sectional profiles calculated using *ab initio* configuration interaction theoretical methods inclusive of vibrational dynamics and contributions from inner-shell excitations in both ground and valence-excited electronic states. The spectra, while broadly similar for all three molecular ions, moved towards lower energies as the number of screening hydrogen atoms increased from one to three. They featured a wide and shallow region below $\sim$107 eV due to $2p \rightarrow \sigma^*$ transitions to dissociative states, and intense and broadened peaks in the $\sim$107–113-eV region merging into sharp Rydberg series due to $2p \rightarrow n\delta, n\pi$ transitions converging on the $L_{II,III}$ limits above $\sim$113 eV. This overall spectral shape is broadly replicated by theory in each case, but the level of agreement does not extend to individual resonance structures. In addition to the fundamental interest, the work should also prove useful for the understanding and modeling of astronomical and laboratory plasma sources where silicon hydride molecular species play significant roles.

I. INTRODUCTION

In a molecule, the electronic relaxation of the core hole created by the photoexcitation (or photoionization) of an inner-shell electron localized on an atomic site, exhibits unique features arising from the related changes in valence electron distributions and their coupling to the nuclear motion degrees of freedom. These interactions may show signatures in the photoabsorption spectra, e.g., in the form of significant broadening effects, and the photoelectron, Auger, x-ray scattering, fluorescence spectra, or (multicoincidence) photoion spectra which characterize the dynamics of the species produced by the decay of the inner-shell vacancy. A significant body of knowledge concerning inner-shell processes has been acquired for shallow core levels in molecules for which typical lifetimes and vibrational characteristic times of a few femtoseconds or more are comparable. The extensive review by Nenner and Morin gives a comprehensive account of many important early works in this area [1] (see also the bibliography assembled by Hitchcock [2]).

More recently, driven by experimental developments in x-ray (1–10 keV) instrumentation at synchrotron radiation facilities [3], the development of femtosecond (fs) and attosecond x-ray sources at free electron laser (FEL) [4] and high-harmonic-generation (HHG) laser [5] facilities, ultrashort studies (sub-fs resolution) have begun. Significant insights into the understanding of molecular core-hole relaxation dynamics have been obtained, for example, the marked effects of photoelectron recoil [6] and postcollision interaction [7] or the ultrafast electronic and dissociation dynamics [8].

The developments and improvements of the theoretical treatments of these effects are ongoing processes and experiments that provide reliable data to benchmark the different theoretical approaches continue to be developed [9].

Considerable progress has been made over the past three decades towards the investigation of inner-shell photoionization cross sections for *atomic* ions; e.g., see reviews [10]. In this regard, *systematic* experimental approaches which enable measurements as functions of, for example, the nuclear charge or the degree of ionization, have proved insightful [11]. In contrast, for *molecular* ions, only a small number of works are known, see [12,13] and references therein, and the *systematic* study of their photoionization behavior remains a largely unexplored field of research.

*Jean-Paul.Mosnier@dcu.ie

The present work focuses on silicon hydride molecular ions, which play significant roles in certain astronomical and technological plasma sources. Silicon-based molecules are a significant trace constituent in late-type stars and star-forming regions, representing nearly 10% of the molecular species identified in space [14]. Silicon hydride molecules, in particular, are of significant astrophysical interest since hydrogen is the most populous atom in the universe. In moving from the bare atomic Si^+ ion to the molecular ions SiH_n^+ ($n = 1,2,3$), one, two, and three neutral hydrogen atoms have been sequentially added. SiH^+ was first observed in the laboratory [15] and reported in the solar photospheric spectrum the same year [16]. SiH^+ has been the subject of several theoretical investigations concentrating on the low-energy valence-excitation region [17]. The SiH^+ solar oscillator strengths [18], photodissociation in interstellar clouds and stellar atmospheres [19], and destruction by chromospheric radiation of Alpha Orionis [20] have been investigated. Until very recently [13], no SiH^+ results were reported for the inner-shell excitation energy regime. A photoionization mass spectrometric study of SiH_n ($n = 1$–4) revealed the appearance of molecular ions SiH_n^+ at different potentials [21], while collision processes involving SiH_n and SiH_n^+ ions with plasma electrons and protons have been studied in hydrogen plasmas [22].

Silicon remains the quintessential semiconductor material in electronic devices, and neutral and ionized silicon atoms and silicon hydride molecules feature in many laboratory plasma processes. For example, the deposition of silicon thin films using plasma-enhanced chemical vapor deposition (PECVD) reactors, with silane (SiH_4) as the process gas, is a key technique to deposit thin-film solar cells. The roles played by the SiH_n ($n = 1$–3) and higher silane radicals in the reactor growth regime have long been recognized as key to optimizing film growth with desired material properties [23].

In this work, we employ a systematic approach to the study of changes in the photoionization behavior of SiH_n^+ ($n = 1,2,3$) molecular ions as we vary the number of bonded hydrogen atoms. *Ab initio* theoretical calculations of the total photoabsorption cross sections are also carried out to support the experiments and provide considerable insight in the interpretation of the experimental spectra.

The present laboratory investigations of molecular-ion *inner-shell* photoionization can benchmark theoretical calculations and provide reliable data for modeling the energy balance and relative ion abundances of astrophysical or laboratory plasma environments where short wavelength sources of radiation play important roles [24]. In star-forming regions, for example, the molecular environment can be strongly influenced by extreme ultraviolet (XUV) and x-ray irradiation [25]. Furthermore, studies of photoionization rates can provide information on the reverse process of radiative recombination, which may be important for understanding the formation and association mechanisms for molecular ions.

II. EXPERIMENTAL DETAILS

The experiments were performed in the energy region of the Si L edge (104–120 eV) with the photon-ion merged-beam setup [26,27] installed on one branch of the PLEIADES beam line at the synchrotron facility SOLEIL [28]. The hydride ions were produced in a permanent magnet electron cyclotron resonance ion source by heating silane (SiH_4) gas with a 12.6-GHz microwave source at a power of less than 1 mW. To extract the ions, a 4-kV bias was applied to the source and charge to mass separation of the ions was performed using a 90° dipole magnet. After collimation by two sets of slits, the selected ions were merged with the counterpropagating monochromatic photon beam in a 0.60-m-long interaction region. The ion current in the region was between 30 and 60 nA.

The synchrotron radiation emitted in the HU80 undulator was monochromatized by a high-flux 600 lines/mm plane grating and a flux of 6.5×10^{13} photons/s was achieved at 120-eV photon energy with 1150 resolving power. The photon flux was systematically monitored using a calibrated Si photodiode. The photon energy was determined using a double-ionization gas cell of Samson type [29]. For the photon energy calibration, we used the $4d \rightarrow 6p$ transition in Xe gas at 65.110 eV, the $3d \rightarrow 5p$ transition in Kr gas at 91.200 eV, and the $2p \rightarrow 3d$ transition in Ar gas at 244.390 eV [30]. The photon energy was corrected for the Doppler shift resulting from the velocity of the SiH_n^+ ions. The estimated accuracy of the absolute photon energy determination is of the order of 30 meV.

An electrostatic lens was placed at the exit of the interaction region between the photon and ion beams to refocus the fragments resulting from Auger decays and molecular dissociations. A second dipole magnet allowed us to separate the produced charged fragments from the incident ion beam. The fragments were counted using 40-mm-diameter microchannel plates while the transmitted (undissociated) beam was collected in a Faraday cup. For each SiH_n^+ ion, a spectrum was obtained from the variation of the intensity of the Si^{2+} fragment as a function of photon energy. A low-frequency chopper (typically 0.1 Hz) was placed in the photon path, before the interaction region, to enable subtraction of the noise produced by background collisional processes (the residual pressure in the interaction chamber was in the 10^{-10} mbar range). Despite the chopper, the strong noise produced by the intense and closely lying SiH_n^+ parent ions prevented the detection of SiH_m^+ ($m = 0$ to n) fragments. Slits placed after the second magnet allowed the mass resolution to be varied. The $^{28}Si^{2+}$ fragments could be resolved from the SiH_m^{2+} close lying fragments, as well as from the $^{29}Si^{2+}$ photoions produced in the photoionization of the isotopic $^{29}Si^+$ ions which were not resolved from the $^{28}SiH^+$ ions by the first magnet. Similarly, no photofragmentation could be detected in the H_m^+ channels likely due to the strong signal produced by background collisional processes.

For the current case of hydrides, the silicon mass is much greater than the mass of the dissociating hydrogens and conservation of energy and momentum calculations for the dissociation of SiH^+ showed that for any reasonable kinetic energy release (KER) value the resulting Si^{2+} ion falls within the collection angle of the detector system [13]. This largely remains the case also for the experiments with SiH_2^+ and SiH_3^+, as the worst-case scenario, whereby successive deviations due to possible successive dissociations would add in the same direction, is unlikely. On the other hand, light fragments such as H^+ or H_2^+ are much less likely to fall within the collection solid angle for detection.

III. THEORETICAL DETAILS

To theoretically replicate the observed silicon hydrides' core-level spectra several steps must be implemented in the calculations: (i) Determination of the excitation energies, including spin-orbit coupling; (ii) Calculation of the transition matrix elements; (iii) Inclusion of the vibrational dynamics, and (iv) Repeat of steps (i)–(iii) to include metastable states.

All the calculations reported in this paper were carried out using the GAMESS-US package and an aug-cc-pVQZ basis set was used for all the ions [31]. Furthermore, the basis set of Si was augmented by additional $s(7)$, $p(6)$, $d(5)$, and $f(3)$ diffuse functions to provide a better description of the Rydberg states.

Our previous work [13] demonstrated the important role played by metastable species in the interpretation of the observed experimental photoionization spectra. In order to evaluate the structural differences between the molecular ions in ground and first metastable states, we have carried out the geometrical optimization for both states for each molecular ion. The calculations were performed within the framework of density functional theory (DFT) using the B3-LYP functional [32]. The accuracy of this method has been tested and validated for many benchmark systems [33]. The same method was also used to calculate the $2p$ ionization potentials neglecting spin-orbit coupling.

The configuration interaction method limited to single excitations (CIS) was employed for the calculation of the core-excited spectra. In spite of the active space limitation to single excitations, this approach provides an accurate description of core-excited states as previously reported [13,34]. The molecular orbitals used in the CI expansion of the core-excited states were computed using the restricted open-shell Hartree-Fock (ROHF) method. The spin-orbit interaction was included through the monoelectronic Breit-Pauli operator [35]. For each core-excited state, the square of the transition dipole moment was computed in the length form as shown in Eq. (1) where $\Psi(0)$ and $\Psi(m)$ are the wave functions for the ground and core-excited states, respectively, and N the number of electrons in the molecular ion.

$$|\vec{\mu}_m|^2 = e \left| \sum_{i=1}^{N} \langle \Psi(m)|r_i|\Psi(0)\rangle \right|^2. \quad (1)$$

The qualitative assignment of the principal transitions was performed through molecular orbitals analysis. Each electronic state is described as a linear combination of a large number of Slater determinants and to assign transitions to these states, we analyzed the character of the determinant having the largest weight. The high number of allowed transitions to highly mixed electronic states within the energy ranges of individual spectral peaks prevents detailed labeling of the resonances. The complexity is compounded by spin-orbit mixing of electronic states of different spin multiplicities. In the *L*-shell threshold region alone (∼15 eV wide), our calculations showed approximately 2000, 3500, and 6000 such transitions for SiH$^+$, SiH$_2$$^+$, and SiH$_3$$^+$, respectively.

For SiH$_2$$^+$ and SiH$_3$$^+$, the inclusion of nuclear dynamics through wave-packet propagation was not affordable because computing the full potential energy surfaces (PES) is not practical. Thus, in order to investigate the broadening related

to the vibrational dynamics of the excited states, we used the linear coupling method [36]. In order to take large vibrational deformations approximately into account, we computed the energy gradient at the equilibrium position in normal coordinates and, then, the coupling constant S_a for each vibrational mode using Eq. (2),

$$S_a = \frac{1}{2\hbar\omega_a^3} \left| \frac{\partial U_a^{\mathrm{ces}}}{\partial q_a} \right|^2, \quad (2)$$

in which ω_a is the frequency of the ath mode and U_a^{ces} is the energy of the core-excited state in the equilibrium geometry. The Franck-Condon factor corresponding to the transition to the ν' vibrational level of the mth core-excited state was computed using the equation

$$|\langle \Psi_{\nu'}(m)|\Psi_{\nu=0}(0)\rangle|^2 = \prod_a \frac{S_a^{\nu'}}{\nu'!} e^{-S_a}, \quad (3)$$

where ν' is the vibrational level of the core-excited state. In cases where the number of significantly populated vibrational levels was large, Gaussian broadening was assumed to simulate the nuclear dynamics in the region of interest, with a full width at half maximum (FWHM) ξ_a related to the gradient of the involved normal mode, as shown in Eq. (4),

$$\xi_a = 2\sqrt{\ln 2}\, \delta q_a \sqrt{\mu_a}\, \alpha_a, \quad (4)$$

where $\alpha_a = \sqrt{h/\mu_a\omega_a}$ is the width of the ground-state nuclear wave function and $\delta q_a = (\frac{\partial U_a^{\mathrm{ces}}}{\partial q_a})\frac{1}{\omega_a^2}$.

The importance of vibrational broadening depends strongly on the particular electronic transition under consideration. For dissociative states, the broadening is usually larger than lifetime and experimental broadening effects (see Sec. IV). For bound electronic states, it depends on the difference between the potential energy surfaces of the ground and core-excited states. In the present case of the Si $2p$ lifetime (45 meV) and an experimental resolution of 80 meV, the nuclear vibrational motions should lead to resolvable vibrational progressions in the electronic spectra. However, in most of the cases discussed below, the details of the vibrational structure are washed out due to the significant spectral overlap between the many broadened individual transitions having very close energies (see above).

Theoretical absorption cross-section spectra were eventually obtained from the calculated energies and transition dipole moments via Voigt profiles as shown in Eq. (5). In this equation n is the number of electronic states and μ_m is the transition dipole moment discussed above. ξ is the FWHM of the profile's Gaussian component taken as the sum of the experimental bandpass (80 meV) and the result of Eq. (4). γ is the FWHM of the profile Lorentzian component equal to the core-hole lifetime (45 meV) of Si$_{2p-1}$ [37].

$$\sigma(\omega) = \sum_{m=1}^{n} \frac{1}{3}\mu_m^2 \int \frac{e^{-(E-\omega)^2/2\xi^2}}{\xi\sqrt{2\pi}}$$

$$\times \frac{\frac{1}{2}\gamma}{\pi\left[(E-\omega-E_m)^2 + \frac{1}{4}\gamma^2\right]} dE. \quad (5)$$

The ratios of the molecular-ion populations in ground and metastable states, as well as the global energy shift between theory and experiment, were evaluated by comparison with
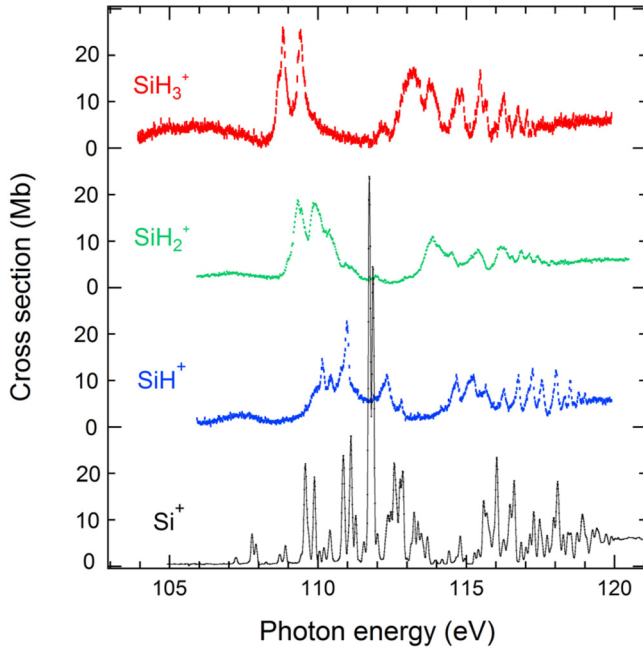
FIG. 1. Measured photoionization cross sections in the 105–120-eV photon energy range for the SiH_n^+ ions, $n = 0$ to 3 (bottom to top). Mb cross-section scales have been obtained assuming the cross-section value at 120-eV photon energy, where direct photoionization in the $2p$ subshell dominates, is the same as that of the known Si^+ ion absolute cross section for all the molecular ions.

the experimental cross sections using a least-squares best fit procedure, optimizing the weight coefficients p_{GS} and p_{MS} for the ground and metastable populations and the total energy shift, respectively.

$$\sigma(\omega) = p_{GS}\sigma_{GS}(\omega) + p_{MS}\sigma_{MS}(\omega). \qquad (6)$$

IV. RESULTS AND ANALYSES

In Fig. 1 we show the evolution of the energy dependence of the experimental photoionization spectra as we move through the Si^+ to SiH_3^+ sequence. The Si^+ cross section was previously experimentally determined on an *absolute* basis (Mb) as reported in an earlier publication [26]. It was not possible to experimentally measure the total photoionization cross section in the same way for the molecular ions, because as described earlier, not all possible channels could be measured. The importance of the complementary measurements for the atomic ion and the molecular ions is that, nevertheless, the former allows us to place the cross sections for the molecular-ion series on an absolute scale also, by making the reasonable assumption that the direct photoionization cross sections at 120-eV photon energy are the same for the Si^+ atomic ion and the silicon hydride ions [13]. This enables us to obtain the Mb scales in Fig. 1 for the interactions of SiH^+, SiH_2^+, and SiH_3^+ molecular ions with photons of energies near the silicon L-shell threshold. The SiH^+ results were reported previously [13] but are shown again here to provide a full overview of the experimental data for the entire Si^+ to SiH_3^+ ion series. The overall appearance of the spectra (Fig. 1) as we move from the atomic ion through the molecular-ion series remains
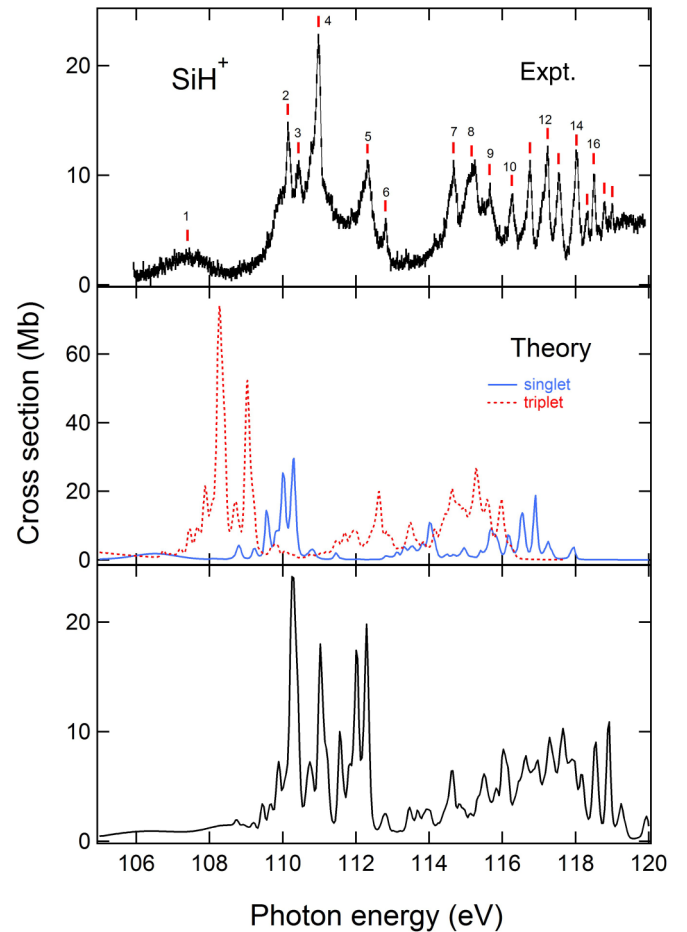

FIG. 2. Photoionization cross sections for the SiH^+ ion in the 105–120-eV photon energy range. Top: Experimental spectrum. The vertical bar on each point represents the statistical uncertainty. Middle: Theoretical spectra for the SiH^+ ion in the ground (blue) and first metastable (red) levels. Bottom: Reconstructed theoretical cross section (see text).

somewhat similar, where we observe a clear systematic trend towards lower energies of the overall spectral shape, as the number of bonded hydrogen atoms increases in the sequence from Si^+ to SiH_3^+. This may be understood qualitatively as arising from the increased screening of the Si nucleus attractive potential due to the additional number of electrons introduced by the increasing number of bonded hydrogen atoms.

In Figs. 2, 3 and 5 we compare, in turn, the experimental results for the SiH_n^+ series ($n = 1$–3) with the corresponding theoretical results comprising both ground-state and metastable-state calculations. The experimental and theoretical plots are placed on the same energy scale. The theoretical results do not take direct ionization processes into account and so the comparisons can only be made for the resonance energy ranges below the ionization energy.

The primary qualitative results are that each molecular ion spectrum divides fairly clearly into distinct regions. (1) A broad and shallow region on the low-energy side (below $\sim$107 eV) that corresponds to the transition of a $2p$ electron to an antibonding molecular orbital σ^*. The $2p \rightarrow \sigma^*$ features as an intense and broad resonance in the spectrum
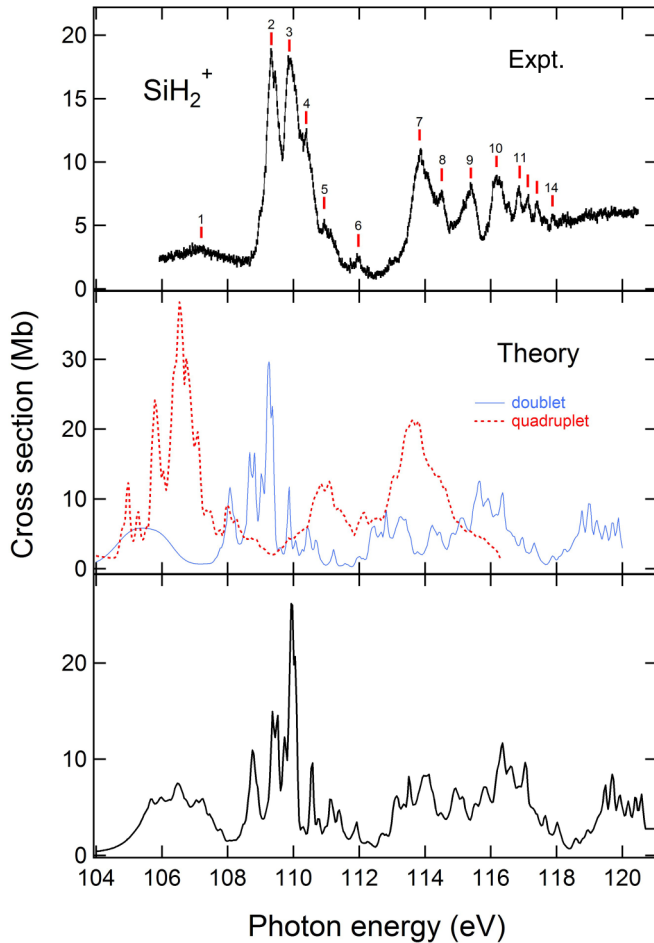
FIG. 3. Photoionization cross sections for the SiH_2^+ ion in the 105–120-eV photon energy range. Top: Experimental spectrum. The vertical bar on each point represents the statistical uncertainty. Middle: Theoretical spectra for the SiH_2^+ ion in the ground (blue) and first metastable (red) levels. Bottom: Reconstructed theoretical cross section (see text).

TABLE I. Energies of the resonance peaks for SiH^+, SiH_2^+, and SiH_3^+ according to the numbering shown in Figs. 2, 3, and 5, respectively.

Peak label	Peak energy (eV) SiH^+	Peak energy (eV) SiH_2^+	Peak energy (eV) SiH_3^+
1	107.4	107.2	105.8
2	110.14	109.33	108.82
3	110.43	109.88	109.41
4	110.98	110.39	112.2
5	112.32	110.94	113.2
6	112.81	111.98	113.8
7	114.67	113.84	114.71
8	115.16	114.51	114.86
9	115.65	115.4	115.47
10	116.26	116.18	115.67
11	116.76	116.88	116.24
12	117.24	117.13	116.44
13	117.54	117.41	116.75
14	118.03	117.88	117.05
15	118.32		
16	118.5		
17	118.79		
18	119.01		

values of which can be used for possible identification of features in the spectra of astrophysical or laboratory sources. Because of the performance limitations of the configuration interaction method, the energy adjustments (i.e., global energy shift) required between the theory and experimental spectra (Figs 2, 3, and 5) depend strongly on the choice of the set of orbitals used in the calculations. SiH^+ and SiH_3^+ have singlet ground electronic states while that of SiH_2^+ is a doublet. A better optimization of the set of orbitals was achieved for the doublet states, which explains the lower-energy shift for SiH_2^+ compared to the other two systems.

For SiH^+ (Fig. 2), the experimental results together with theoretical spectra obtained in the wave-packet propagation approach for the nuclear dynamics were previously reported in [13]. As explained in Sec. III, such an approach goes beyond the linear coupling model used here to simulate the nuclear dynamics for the larger ions SiH_2^+ and SiH_3^+. We now present in Fig. 2 the SiH^+ theoretical spectra obtained using the same linear coupling theoretical approach as that used for SiH_2^+ and SiH_3^+. The linear coupling model reproduces quite well the more accurate wave-packet calculations [13] for SiH^+, which gives us confidence that the linear coupling method can be used for all the systems considered here. As mentioned earlier, the most significant nuclear motion effects appear when the core-excited state is dissociative leading to large broadening of the corresponding peak. Even at the modest level of agreement between theory and experiment shown in Figs. 2, 3, and 5 the comparison clearly allows the separation of dissociative and bound states. The very broad dissociative features in each molecular-ion spectrum in the 105–108-eV spectral region are substantially broader in character than the bound-state features at higher energies. The calculated broadening, see Eqs. (4) and (5), of the dissociative states, due to the nuclear dynamics,

of silane which has been extensively studied [38]. The final inner-shell electronically excited states of the transition are dissociative and the underlying structure and overall shape of this spectral feature depend critically on the vibrational nuclear dynamics. (2) A strong "valence-excitation" region (moving approximately from about 112 eV for the bare Si^+ ion to about 109 eV for SiH_3^+) that would correspond to $2p \rightarrow 3d$ inner-shell transitions in the P^+, S^+, and Cl^+ united atoms for the SiH^+, SiH_2^+, and SiH_3^+ molecules, respectively. (3) An extended Rydberg series of resonances found on the high-photon-energy side of each spectrum (above ∼112 eV) corresponding to $2p \rightarrow n\delta, n\pi$ transitions converging on the $L_{II,III}$ ionization limits. The overall experimental spectral shape is broadly replicated by theory in each case (Figs. 2, 3, and 5) but the level of agreement does not extend to individual resonance structures. While detailed spectral assignments are not possible for the reasons indicated earlier, comparing the middle and lower panels of Figs. 2, 3, and 5 allows the association of most of the strong experimental features with either the ground or metastable initial state. Table I shows the energies of the dominant resonances for each ion, the

ranged between 0.9 and 2 eV, depending on the molecular ion and whether the transition originated in the ground or metastable state.

We now give more specific details for each molecular ion. The ground state of SiH$^+$ is $X\,^1\Sigma^+$ and the main structures observed in the 106–112-eV energy region arise from the excitation of an atomiclike $2p$ electron to empty molecular orbitals of $3d$ atomic character. Inner-shell excitations from the $X\,^1\Sigma^+$ electronic ground state explain many of the spectral features but some notable differences remain, however, requiring inclusion of resonances due to inner-shell excitations from the metastable $a\,^3\Pi$ triplet state, which lies 2.29 eV above the ground state and remained populated within the interaction region. The calculated internuclear equilibrium distances for the ground and metastable states are computed at 0.1514 and 0.1547 nm, respectively, compared to the experimental length of 0.1504 nm [39]. As briefly noted earlier, in order to find the optimum mix of ground and excited states to represent the experimental data, we performed a least-squares best fitting of the theoretical results adjusting the ground- and excited-state population ratio coefficients p_{GS} and p_{MS} [Eq. (6)] and also the energy shift between theory and experiment. Optimum agreement was achieved if the synthetic SiH$^+$ spectrum included $\sim$35% fraction of the $a\,^3\Pi$ state and a global energy shift of $\sim$2.0 eV. The bottom part of Fig. 2 shows the results of this procedure, which can be compared to the experimental data in the top part. The importance of complementary calculations providing resonance information for both ground and excited metastable states for the interpretation of the spectra is clear. Above 113-eV up to about 120-eV photon energies, $2p$ inner-shell excitations to highly excited molecular states form characteristic converging Rydberg series leading to ionization limits separated by approximately the silicon 0.65-eV $L_{\mathrm{II,III}}$ spin-orbit splitting, analogous to the case of silane [40]. The calculated ionization potential for the $2p$ subshell neglecting spin-orbit interactions is 119.5 eV.

The corresponding comparisons for SiH$_2^+$ are shown in Fig. 3. Detection of the bare Si^{2+} ions in this case requires the loss of both hydrogens. The ground electronic state of SiH$_2^+$ is a $^2A_1$ doublet state while the lowest metastable state is a quadruplet state and lies 3.7 eV above the ground state. The theoretical optimization results show substantially different geometries, as illustrated in Fig. 4, between the ground state (Si-H bond length 0.148 nm and interbond angle 119.5°) and the metastable state (Si-H bond length 0.160 nm and interbond angle 69°). The ionization thresholds were computed at 116.8 and 115.9 eV, respectively, neglecting spin-orbit coupling. The best fit shown in the bottom panel of Fig. 3 was obtained with an approximate 9:1 ratio of ground to metastable and a global energy shift of $\sim$0.7 eV.

The ground electronic state of SiH$_3^+$ is $^1A_1$ while the triplet metastable state lies at 3.02 eV. The calculated ionization potentials are 116.9 and 116.8 eV, respectively. In strong contrast to the two previous cases the computed optimum fit between the experimental data and the theoretical spectra implies that the majority ($\sim$80%) of the molecular ions are in the excited metastable state (see Fig. 5). The required energy shift was $\sim$3.3 eV. It is interesting to note that in the case of SiH$_3^+$ the computed geometries for the ground and metastable electronic states are very different. Both ground-
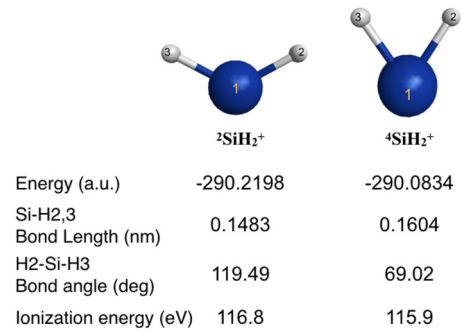

FIG. 4. Calculated equilibrium geometry, electronic energy (atomic units) and L-shell ionization energies (eV) for the ground doublet ^{2}SiH$_2^+$ and first metastable quadruplet ^{4}SiH$_2^+$ electronic states of the SiH$_2^+$ molecular ion, respectively.

	^{2}SiH$_2^+$	^{4}SiH$_2^+$
Energy (a.u.)	-290.2198	-290.0834
Si-H2,3 Bond Length (nm)	0.1483	0.1604
H2-Si-H3 Bond angle (deg)	119.49	69.02
Ionization energy (eV)	116.8	115.9

and metastable-state shapes are illustrated in Fig. 6. The calculated ground-state shape is highly symmetrical with all three hydrogens in an equilateral triangle formation, with a silicon-hydrogen bond length of 0.1467 nm and an angle of
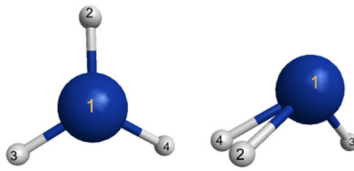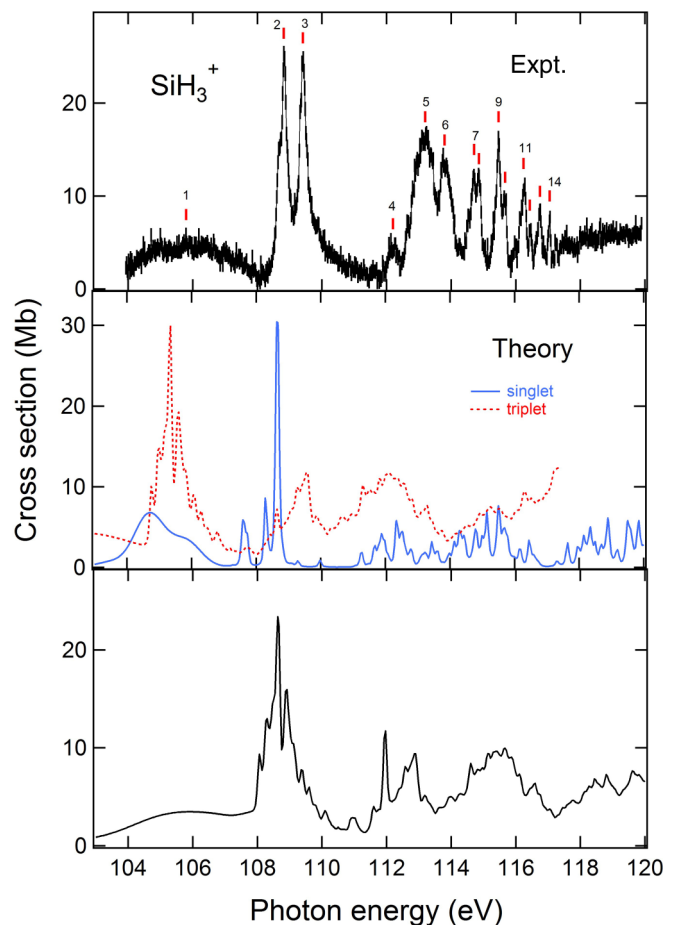

FIG. 5. Photoionization cross sections for the SiH$_3^+$ ion in the 105–120-eV photon energy range. Top: Experimental spectrum. The vertical bar on each point represents the statistical uncertainty. Middle: Theoretical spectra for the SiH$_3^+$ ion in the ground (blue) and first metastable (red) levels. Bottom: Reconstructed theoretical cross section (see text).

	$^1SiH_3{}^+$	$^3SiH_3{}^+$
Energy (a.u.)	-290.9141	-290.8031
Si-H2,4 Bond Length (nm)	0.1467	0.1713
Si-H3 Bond Length (nm)	0.1467	0.1490
H3-Si-H2,4 Bond angle (deg)	120	105.4
H2-Si-H4 Bond angle (deg)	120	29.03
Ionization energy (eV)	116.9	116.8

FIG. 6. Calculated equilibrium geometry, electronic energy (atomic units), and *L*-shell ionization energies (eV) for the ground singlet $^1SiH_3{}^+$ and first metastable triplet $^3SiH_3{}^+$ electronic states of the $SiH_3{}^+$ molecular ion, respectively.

120° between the bonds. This contrasts sharply with the highly asymmetrical arrangement for the triplet metastable state. The two further-out hydrogens in the metastable state are both 0.1713 nm, while the third hydrogen is 0.1490 nm, respectively,

TABLE II. Assignment of the dominant excitation schemes for the $2p$ inner-shell electron to either empty or singly occupied outer molecular orbital states in the *L*-shell photoabsorption spectra of the SiH^+, $SiH_2{}^+$, and $SiH_3{}^+$ molecules in their ground and their first metastable states.

| Molecule	Photon energy range (eV)	$2p$ electron excitation
$^1SiH^+$	<104.0	$2p \rightarrow 2\pi$
	102–108.2	$2p \rightarrow 1 - 2\sigma^*$
	108.2–113	$2p \rightarrow n\delta, n\pi$ (strong configuration mixing)
	<113	$2p \rightarrow$ Rydberg
$^3SiH^+$	<98.0	$2p \rightarrow 2\pi$ (singly occupied MOs)
	99.0–104.0	$2p \rightarrow 1 - 2\sigma^*$
	104–108	$2p \rightarrow n\delta, n\pi$ (strong configuration mixing)
	>108	$2p \rightarrow$ Rydberg
$^2SiH_2{}^+$	95.0–102.0	$2p \rightarrow 5a_1$ (singly occupied MO)
	102–107.0	$2p \rightarrow 6a_1, 4 - 1a_2$
	107–112	$2p \rightarrow 7a_1, 4 - 5a_2$
	>112.0	$2p \rightarrow$ Rydberg
$^4SiH_2{}^+$	95.0–98.8	$2p \rightarrow 5a_1, 3b_1$ (singly occupied MOs)
	98.8–108.0	$2p \rightarrow 6 - 7a_1$
	108.0–113.0	$2p \rightarrow 3 - 4a_2$
	>113	$2p \rightarrow$ Rydberg
$^1SiH_3{}^+$	<106.5	$2p \rightarrow 5a_1', 3e'$
	106.5–113	$2p \rightarrow 6a_1', 5e'$
	>113	$2p \rightarrow$ Rydberg
$^3SiH_3{}^+$	<98.0	$2p \rightarrow 2 - 3a''$ (singly occupied MOs)
	98.0–107.0	$2p \rightarrow 7 - 8a'$
	>107.0	Highly mixed
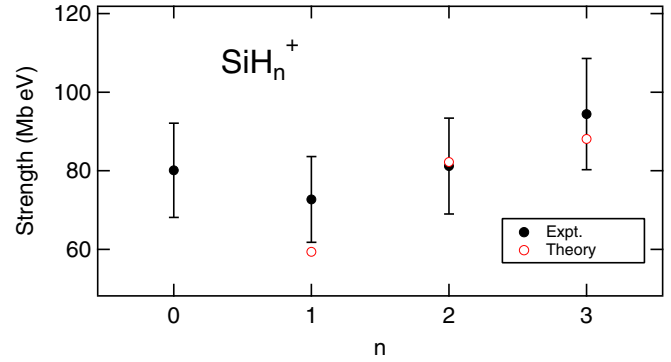
FIG. 7. Experimental and theoretical cross sections integrated between 105 and 120 eV for the $SiH_n{}^+$ ions ($n = 0, 1, 2, 3$).

from the silicon. The angle between the two further-out hydrogen-silicon bonds is 29° while the third hydrogen-silicon bond lies at 105.4°. It may be the case that the geometrical arrangement of the metastable state favors its production in the various excitation and deexcitation processes occurring in the electron cyclotron resonance plasma (ECR) source and its subsequent longevity.

While the high-energy densities of molecular resonances prevented detailed discrete spectral peak assignments, theory does provide some insight in terms of broad assignments within different energy regions for each ion. In Table II, we provide overviews of the dominant one-electron transition assignments obtained without spin-orbit coupling.

Finally, we remarked earlier that a particular problem in measuring the cross section for molecular ions is related to the difficulty in quantifying the absolute cross sections in the same way as for atomic ions. In this work, we used normalization to the experimentally determined absolute cross section for the atomic ion Si^+ at 120 eV to estimate the corresponding absolute cross sections for the molecular ions. If we sum the resulting cross sections (Fig. 1) for each ion species between 105 and 120 eV we find the values $\sim$80 Mb eV for Si^+, $\sim$72 Mb eV for SiH^+, $\sim$78 Mb eV for $SiH_2{}^+$, and $\sim$91 Mb eV for $SiH_3{}^+$ as shown in Fig. 7. Taking the error bars into account ($\pm$15%), these values are fairly consistent, providing evidence of the reasonableness of the normalization procedure. The corresponding points for the integration of the theoretical cross sections (Fig. 7) over the same energy interval show similar consistency and are in fair agreement with the experimental values.

V. CONCLUSIONS

Inner-shell excitations play a critical role in the interaction of photons in the soft x-ray and x-ray spectral regions with atomic and molecular ions. We have coupled monochromatized synchrotron radiation with an ECR plasma molecular-ion source in a merged-beam configuration, to systematically explore the behavior of the Si inner-shell photoionization cross section in diatomic and polyatomic molecular $SiH_n{}^+$ ions as the number of screening hydrogen atoms is varied. Our results indicate that competition between Auger decay and nuclear dissociation is relatively independent of the number of bonded hydrogens and the dominant decay channel in each case leads to Si^{2+}. All species demonstrated clear valence-excitation

regions and extended Rydberg series leading to ionization limits which move to lower photon energies as the number of bonded hydrogen atoms increases. The molecular cross sections were put on an absolute scale, by comparison with the corresponding measurements for the parent Si^+ atomic ion. The experimental data have been interpreted by comparison with the predictions of our *ab initio* theoretical calculations. Theoretical absorption cross-section spectra were obtained from the calculated energies and transition dipole moments. Intercomparison between the experimental and theoretical data shows that photoexcitation from both ground and valence-excited metastable electronic states needs to be taken into account and allows calculation of the ratios between ground-state and excited-state configurations originating in the ECR source. Geometrical optimization within the density functional theoretical framework allowed structural differences between the molecular ions in the ground and excited states to be identified in each case. Significant structural differences between ground and excited states are shown to exist particularly in the polyatomic cases. Very broad dissociative features were observed in each molecular-ion spectrum with associated calculated nuclear dynamic broadening in the $\sim$1–2 eV range.

While general agreement between theory and experiment has been shown to exist at the overall qualitative level, detailed agreement will demand further efforts, illustrating the continuing importance of the provision of experimental data to help benchmark theoretical advances. For molecular ions, the fewer symmetries when compared to atomic ions, and the increased nuclear degrees of freedom, add to the theoretical challenge.

The energies and photoexcitation cross sections of the main L-shell resonances were measured for each molecular ion. The experimental and theoretical data will help with the identification of these molecules in astronomical sources and laboratory plasmas and will also aid the modeling of the species abundance and dynamics.

[1] I. Nenner and P. Morin, in *VUV and Soft X-Ray Photoionization*, edited by U. Becker and D. A. Shirley (Plenum Press, New York, 1996), Chap. 9.

[2] A. P. Hitchcock, http://unicorn.mcmaster.ca/corex.html (2003).

[3] M. N. Piancastelli, R. Guillemin, T. Marchenko, L. Journel, O. Travnikova, T. Marin, G. Goldsztejn, B. Cunha de Miranda, I. Ismail, and M. Simon, J. Phys. B **50**, 042001 (2017).

[4] K. C. Prince, E. Allaria, C. Callegari, R. Cucini, G. De Ninno, S. Di Mitri, B. Diviacco, E. Ferrari, P. Finetti, and D. Gauthier *et al.*, Nat. Photonics **10**, 176 (2016).

[5] S. M. Teichmann, F. Silva, S. L. Cousin, M. Hemmer, and J. Biegert, Nat. Commun. **7**, 11493 (2016).

[6] E. Kukk, T. D. Thomas, K. Ueda, D. Ceolin, S. Granroth, K. Kooser, O. Travnikova, D. Iablonsky, P. Decleva, D. Ayuso, R. Püttner, H. Levola, G. Goldsztejn, T. Marchenko, M. Piancastelli, and M. Simon, Phys. Rev. A **95**, 042509 (2017).

[7] R. Guillemin, S. Sheinerman, T. Marin, L. Journel, T. Marchenko, R. K. Kushawaha, N. Trcera, M. N. Piancastelli, and M. Simon, J. Phys. B **46**, 215101 (2013).

[8] O. Travnikova, T. Marchenko, G. Goldsztejn, K. Jänkälä, N. Sisourat, S. Carniato, R. Guillemin, L. Journel, D. Céolin, R. Püttner, H. Iwayama, E. Shigemasa, M. N. Piancastelli, and M. Simon, Phys. Rev. Lett. **116**, 213001 (2016); C. S. Lehmann, A. Picón, C. Bostedt, A. Rudenko, A. Marinelli, D. Moonshiram, T. Osipov, D. Rolles, N. Berrah, C. Bomme, M. Bucher, G. Doumy, B. Erk, K. R. Ferguson, T. Gorkhover, P. J. Ho, E. P. Kanter, B. Krassig, J. Krzywinski, A. A. Lutman *et al.*, Phys. Rev. A **94**, 013426 (2016); C.-T. Liao, X. Li, D. J. Haxton, T. N. Rescigno, R. R. Lucchese, C. W. McCurdy, and A. Sandhu, *ibid.* **95**, 043427 (2017).

[9] R. Bohinc, M. Žitnik, K. Bučar, and M. Kavčič, J. Chem. Phys. **140**, 164304 (2014); T. Marchenko, S. Carniato, L. Journel, R. Guillemin, E. Kawerk, M. Žitnik, M. Kavčič, K. Bučar, R. Bohinc, M. Petric, V. Vaz da Cruz, F. Gel'mukhanov, and M. Simon, Phys. Rev. X **5**, 031021 (2015).

[10] J. B. West, J. Phys. B **34**, R45 (2001); H. Kjeldsen, **39**, R325 (2006); S. Schippers, A. L. D. Kylcoyne, R. A. Phaneuf, and A. Müller, Contemp. Phys. **57**, 215 (2016); R. Smith, J.-M. Li, A. Müller, and F. Salama, J. Phys. B **50**, 060201 (2017).

[11] H. S. Chakraborty, A. Gray, J. T. Costello, P. C. Deshmukh, G. N. Haque, E. T. Kennedy, S. T. Manson, and J. P. Mosnier, Phys. Rev. Lett. **83**, 2151 (1999); J.-M. Bizau, D. Cubaynes, J.-M. Esteva, F. J. Wuilleumier, C. Blancard, J. Bruneau, J.-P. Champeaux, A. Compant La Fontaine, C. Couillaud, R. Marmoret, C. Rémond, D. Hitz, M. Delaunay, N. Haque, P. C. Deshmukh, H. L. Zhou, and S. T. Manson, *ibid.* **87**, 273002 (2001); E. T. Kennedy, J. T. Costello, J. P. Mosnier, and P. Van Kampen, Radiat. Phys. Chem. **70**, 291 (2004); A. Müller, S. Schippers, J. Helhund, A. L. D. Kylcoyne, R. A. Phaneuf, and B. M. McLaughlin, J. Phys. B **50**, 085007 (2017).

[12] A. Müller, S. Schippers, M. Habibi, D. Esteves, J. C. Wang, R. A. Phaneuf, A. L. D. Kilcoyne, A. Aguilar, and L. Dunsch, Phys. Rev. Lett. **101**, 133001 (2008); T. Andersen, H. Kjeldsen, H. Knuden, and F. Folkmann, J. Phys. B **34**, L327 (2001); J. Hellhund, A. Borovik, Jr., K. Holste, S. Klumpp, M. Martins, S. Ricz, S. Schippers, and A. Müller, Phys. Rev. A **92**, 013413 (2015); D. S. Belic, X. Urbain, H. Cherkani-Hassani, and P. Defrance, *ibid.* **95**, 052702 (2017); J. Lecointre, D. S. Belic, J. J. Jureta, R. Janev, and P. Defrance, Eur. J. Phys. D **50**, 265 (2008).

[13] J.-P. Mosnier, E. T. Kennedy, P. van Kampen, D. Cubaynes, S. Guilbaud, N. Sisourat, A. Puglisi, S. Carniato, and J.-M. Bizau, Phys. Rev. A **93**, 061401(R) (2016).

[14] M. C. McCarthy, C. A. Gottlieb, and P. Thaddeus, Mol. Phys. **101**, 697 (2003).

[15] A. F. Douglas and B. L. Lutz, Can. J. Phys. **48**, 247 (1970).

[16] N. Grevesse and A. J. Sauval, Astron. Astrophys. **9**, 232 (1970).

[17] B. Sannigrahi, R. J. Buenker, G. Hirsch, and J.-P. Gu, Chem. Phys. Lett. **237**, 204 (1995); J. Whitham, J. M. Walmsley, T. E. Masters, A. Geers, T. Gibbon, Y. Chen, and P. J. Sarre, J. Chem. Soc., Faraday Trans. **93**, 1705 (1997).

[18] C. Trivedi and K. Sinha, J. Korean Astron. Soc. **29**, S345 (1996); N. Grevesse and A. J. Sauval, J. Quant. Spectrosc. Radiat. Transfer **11**, 65 (1971).

[19] P. C. Stancil, K. Kirby, A. B. Sannigrahi, R. J. Buenker, G. Hirsch, and J.-P. Gu, Astrophys. J. **486**, 574 (1997); K. Kirby, W. G. Roberge, R. P. Saxon, and B. Liu, *ibid.* **239**, 855 (1980).

[20] J. Wirsch, Astrophys. J. **331**, 463 (1988).

[21] J. Berkowitz, J. P. Greene, H. Cho, and B Ruscic, J. Chem. Phys. **86**, 1235 (1987).

[22] R. K. Janev and D. Reiter, Contrib. Plasma Phys. **43**, 401 (2003).

[23] L. Guo, M. Kondo, M. Fukawa, K. Saitoh, and A. Matsuda, Jpn. J. Appl. Phys. **37**, L1116 (1998); T. Roschek, T. Repmann, J. Müller, B. Rech, and H. Wagner, J. Vac. Sci. Technol. A **20**, 492 (2002); S. G. Sayres, M. W. Ross, and A. W. Castleman, Jr., Phys. Rev. A **82**, 033424 (2010).

[24] E. Gatuzz, J. Garca, T. R. Kallman, C. Mendoza, and T. W. Gorczyca, Astrophys. J. **800**, 29 (2015); R. Meijerink and M. Spaans, Astron. Astrophys. **436**, 397 (2005).

[25] A. O. Benz, S. Bruderer, E. F. Van Dishoek, P. Stäuber, and S. F. Wampfler, J. Phys. Chem. A **117**, 9840 (2013); P. Stäuber, S. D. Doty, E. F. Van Dishoek, and A. O. Benz, Astron. Astrophys. **440**, 949 (2005); P. R. Maloney, D. J. Hollenbach, and A. G. G. M. Tielens, Astrophys. J. **466**, 561 (1996); J. Wilms, A. Allen, and R. McCray, *ibid.* **542**, 914 (2000); B. Ercolano, C. J. Clarke, and J. J. Drake, *ibid.* **699**, 1639 (2009).

[26] E. T. Kennedy, J.-P. Mosnier, P. Van Kampen, D. Cubaynes, S. Guilbaud, C. Blancard, B. M. McLaughlin, and J.-M. Bizau, Phys. Rev. A **90**, 063409 (2014).

[27] J. M. Bizau, D. Cubaynes, S. Guilbaud, N. El Eassan, M. M. Al Shorman, E. Bouisset, J. Guigand, O. Moustier, A. Marié, E. Nadal, E. Robert, C. Nicolas, and C. Miron, J. Electron Spectrosc. Relat. Phenom. **210**, 5 (2016).

[28] C. Miron, C. Nicolas, and E. Robert, http://www.synchrotronsoleil.fr/Recherche/LignesLumiere/PLEIADES.

[29] J. A. R. Samson, *Techniques of Vacuum Ultraviolet Spectroscopy* (John Wiley & Sons, New York, 1967).

[30] C. G. King, M. Tronc, F. Read, and R. C. Bradford, J. Phys. B: At. Mol. Phys. **10**, 2479 (1977).

[31] M. W. Schmidt, K. K. Baldridge, J. A. Boatz, S. T. Elbert, M. S. Gordon, J. H. Jensen, S. Koseki, N. Matsunaga, K. A. Nguyen, S. Su, T. L. Windus, M. Dupuis, and J. A. Montgomery, J. Comput. Chem. **14**, 1347 (1993).

[32] K. Kim and K. D. Jordan, J. Phys. Chem. **98**, 10089 (1994).

[33] A. El-Azhary and H. U. Suter, J. Phys. Chem. **100**, 15056 (1996); J. A. Montgomery, Jr., M. J. Frisch, J. W. Ochterski, and G. A. Petersson, J. Chem. Phys. **110**, 2822 (1999).

[34] A. Puglisi, N. Sisourat, and S. Carniato, Atomic Processes in Plasmas APIP 2016—2016, Paris, Proceedings of the 18th and 19th International Conference on Atomic Processes in Plasmas, AIP Conf. Proc. No. 1811, edited by D. Benredjem 130002 (AIP, New York, 2017).

[35] D. G. Fedorov and M. S. Gordon, J. Chem. Phys. **112**, 5611 (2000).

[36] T. E. Sharp and H. M. Resenstock, J. Chem. Phys. **41**, 3453 (1964); E. V. Doktorov, A. Malkin, and V. I. Manko, J. Mol. Spectrosc. **56**, 1 (1975).

[37] J. D. Bozek, G. M. Bancroft, J. N. Cutler, and K. H. Tan, Phys. Rev. Lett. **65**, 2757 (1990); J. D. Bozek, G. M. Bancroft, and K. H. Tan, Phys. Rev. A **43**, 3597 (1991).

[38] G. G. B. de Souza, P. Morin, and I. Nenner, Phys. Rev. A **34**, 4770 (1986); A. Yagishita, S. Arai, C. E. Brion, T. Hayaishi, J. Murakami, Y. Sato, and M. Ukai, Chem. Phys. Lett. **132**, 437 (1986); Y. Sato, K. Ueda, A. Yagishita, T. Sasaki, T. Nagata, T. Hayaishi, M. Yoshino, T. Koizumi, and A. A. McDowell, Phys. Scr. **41**, 55 (1990).

[39] P. J. Linstrom and W. G. Mallard (Eds.), *NIST Chemistry WebBook*, NIST Standard Reference Database No. 69 (US Secretary of Commerce, Washington, DC, 2017).

[40] W. Hayes and F. C. Brown, Phys. Rev. A **6**, 21 (1972).